JOURNAL OF PROPULSION AND POWER
Vol. 15, No. 4, July–August 1999

Drags in Scramjet Engine Testing: Experimental and Computational Fluid Dynamics Studies

Tohru Mitani,* Takeshi Kanda,† and Tetsuo Hiraiwa‡
National Aerospace Laboratory, Miyagi 981-1525, Japan
and
Yasutaka Igarashi§ and Kazuhiro Nakahashi¶
Tohoku University, Miyagi 980-0845, Japan

No-fuel internal drag of a side-compression scramjet engine was evaluated by using two one-fifth-subscaled models, one for wall pressure measurement and the other for force measurement under conditions of a flight Mach number of 4. The pressure and frictional drags in various parts of the models were estimated from these wind-tunnel tests. Comparison between the pressure measurement and the force measurement revealed that the drag derived by these wind-tunnel tests agreed within 5%. After examining the consistency between the pressure and the force experiments, these results were used to calibrate a newly developed computational fluid dynamics code. The frictional drag and the heating rate on the engine internal walls were evaluated with the unstructured-grid code to be compared with those obtained from the one-fifth-subscale model and the full-scale engine. The total drag coefficient of the scramjet engine, including the installation drag, was found to be 0.281 and the internal drag coefficient was found to be 0.093. Consequently, two-thirds of the total drag measured in engine testing in the Ramjet Engine Test Facility was produced by the external flow over the engine module. Subtracting the external drag, the internal performance delivered by the H_2-fueled scramjet engine is discussed.

Nomenclature

Cd_f = frictional drag coefficient
Cd_p = pressure drag coefficient
c_f = skin-friction coefficient
D_{ext} = engine external drag
D_{int} = engine internal drag
D_{ttl} = total engine drag, $D_{\text{int}} + D_{\text{ext}}$
F_{LC} = force indicated by load cell, D_{ttl} + installation drag $+\Delta F$
M = Mach number
P_w = wall pressure
P_0 = total pressure
q = local dynamic pressure
q_w = wall heating rate
Re_L = Reynolds number for length, L
T_{int} = engine internal thrust, $D_{\text{int}} + \Delta F$
T_0 = total temperature
γ = specific heat
ΔF = thrust increment by combustion
υ_w = local wall friction

Introduction

THE Kakuda Research Center at the National Aerospace Laboratory, Japan, is testing H_2-fueled scramjet engines in the Ramjet Engine Test Facility (RJTF).[1–3] The typical engine configuration and dimensions are shown in Fig. 1. The H_2-fueled scramjet engine is rectangular with a length of 2.1 m. It consists of a cowl, a top wall, and two side walls. The entrance and the exit of the engine are 200 mm wide and 250 mm high. The side-wall-compression-type inlet has 6-deg half-angle wedges, and the leading edges are swept back by 45 deg to deflect the airstream for spillage. The H_2 is injected normal from the side walls, or tangentially to the side walls. Various fuel struts were compared in the $M6$ and $M8$ tests, although no strut was attached in the $M4$ tests discussed here. The combustion gas was expanded and accelerated through the diverging combustor and the nozzle. Thrust increment overcoming the engine drag was observed in the $M4$ and $M6$ tests.

The scramjet engine suffers large drag caused by compression and spillage of air in the inlet without fuel injection (no-fuel engine internal drag D_{int}). Consequently, the net thrust to propel vehicles is reduced. Accurate estimation of the D_{int} is essential to assess the feasibility of the system flying in the hypersonic regime.[3–5] Voland[5] reported good agreement of D_{int} between two experimental methods (wall pressure measurement and momentum balance measurement) for NASA Lewis Research Center's strutless scramjet in the Mach 6 freestream.

However, the application of computational fluid dynamics (CFD) to the internal flow of the engine was not successful.[6] Duman et al.[7] applied CFD with various turbulent models to two inlets and pointed out that the CFD was able to detect the trend found in the experiments, but that the prediction of heat flux was difficult. A case study of CFD applied to hypersonic vehicles and propulsion systems was presented by Barber and Cox.[8] Because experiments in hypersonic propulsion are inevitably pointwise as a result of the limited ground-testing facilities, CFD should complement and extend those experimental results. After comprehensive calibrations of CFD codes by use of the experimental data, it is possible to apply the CFD codes to more general engine configurations and flight conditions.

The main objective of this paper is to access the validity and accuracy of CFD for the internal flow in scramjet engines, not only with the pressure distributions, but also with the transport properties such as frictional drag and heating rate. At first, wall pressure and force balance experiments were conducted using one-fifth-subscale models of the scramjet engine tested in the RJTF under $M4$ flight conditions (the inlet Mach number was 3.4). The pressure and the friction drags were estimated and the D_{int} and engine external

Presented as Paper 98-1512 at the AIAA 8th International Space Planes and Hypersonic Systems and Technologies Conference, Norfolk, VA, 27–30 April 1998; received 24 July 1998; revision received 12 November 1998; accepted for publication 12 November 1998.

*Chief of Ramjet Combustion Section, Kakuda Research Center, Ramjet Propulsion Division, Kimigaya, Kakuda.
†Chief of Ramjet System Section, Kakuda Research Center, Ramjet Propulsion Division, Kimigaya, Kakuda.
‡Researcher, Kakuda Research Center, Ramjet Propulsion Division, Kimigaya, Kakuda.
§Graduate Student, Department of Aeronautics and Space Engineering, Sendai.
¶Professor, Department of Aeronautics and Space Engineering, Sendai.

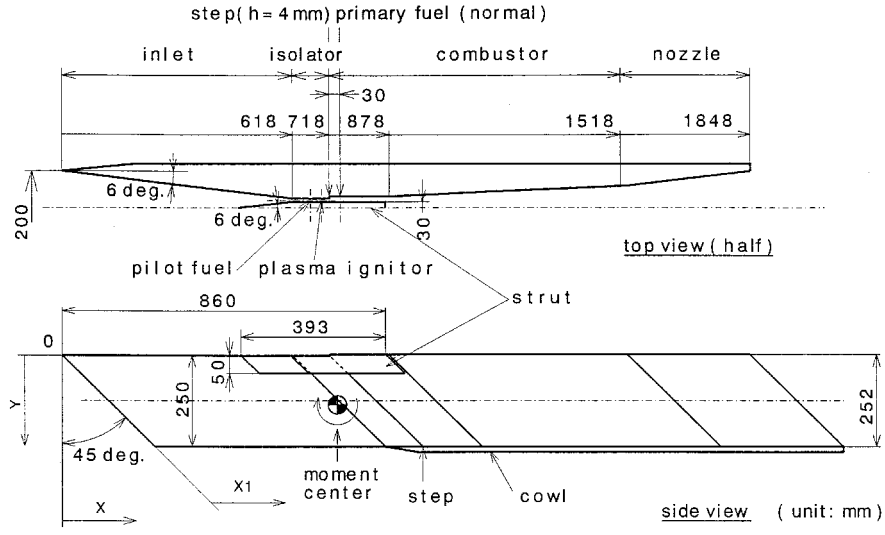

Fig. 1 H_2-fueled scramjet engine tested in the RJTF.

drag (D_{ext}) were separated. Then, the flowfield inside of the model was numerically computed using a newly developed, unstructured grid flow solver for three-dimensional Reynolds-averaged Navier–Stokes equations.[9] The CFD results on pressure distributions, the pressure and friction drags, and the heat transfer rate were compared with the experimental data. Finally, the internal thrust and specific impulse of the H_2-fueled scramjet engine tested in the RJTF were examined based on the drags found here.

Wind-Tunnel Testing

Wall Pressure and Force Experiments

A subscale wind tunnel with a 102-mm-square nozzle exit was utilized. This wind tunnel was a freejet type at a scale exactly one-fifth of the RJTF engine wind tunnel. Because the air does not condense in the $M3.4$ flow with $T_0 = 290$ K, room-temperature air was used in this experiment. The typical Reynolds number was 2.4×10^7, with respect to the model length (0.42 m) and $P_0 = 2$ MPa. Using an air-ejector system to lower the test cell pressure, the Reynolds number can be controlled from 3×10^6 to 3×10^7 through the P_0 control in this one-fifth-scale wind tunnel.

Two one-fifth-scale models (flow path dimensions = 40 mm wide, 50 mm high and 420 mm long) of the scramjet engine shown in Fig. 1 were constructed: a model for the wall pressure (P_w) measurement and a model for the force balance measurement. The wall pressure model was constructed to only reproduce the internal flow geometry, and it was instrumented with P_w pressure taps at ~140 locations (typically, 100 on the side wall, 27 on the top wall, 10 on the cowl, and 5 on the engine strut). The force model, duplicating the external geometry as well as the internal geometry, was suspended from the support strut with a diamond cross section on the axial force measuring system (Fig. 2).

The model was designed to divide a support strut, two side walls, a cowl, and an engine strut to itemize the individual drags by a strain-gauge load cell using a component buildup process. A windshield (fairing) was prepared to cover the support strut from the freestream. The drag on the fairing was transferred to the engine model when the engine tests in the RJTF were simulated with the one-fifth-subscale model. When itemizing the drags on the supporting strut or on the fairing, the fairing was attached to the test cell so that the drag on the supporting strut was not added to the load-cell reading. In addition, it was possible to segment the side walls into the inlet section and the downstream section to measure the drag on the inlet compression section, as illustrated in Fig. 2.

In the force model, pressures at a limited number of stations on the walls were measured so that the pressure tubes did not disturb the freestream. All of the pressure tubes were contained in the support strut. The alignment of the model to the $M3.4$ flow was monitored

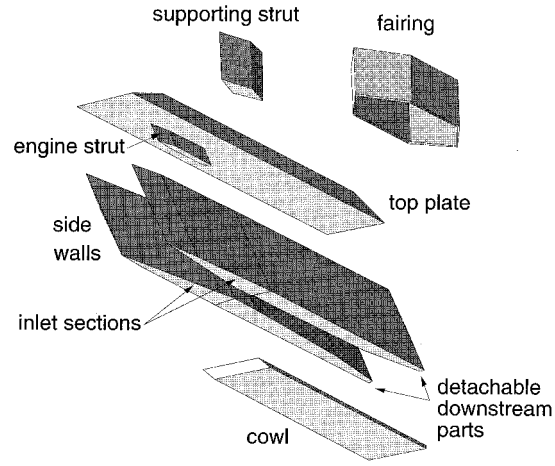

Fig. 2 One-fifth-subscale model for engine drag measurement. The individual drags of components were itemized by a component buildup process.

by internal wall pressures. The pressure drag on the top plate was estimated by the pressure difference between the external wedges measured at the upstream and the downstream walls of the top plate. Several pitot pressures were measured on the support strut.

Pressure and Frictional Drags

The P_w distributions on the model inner walls were obtained by measurements at 26 locations on the top plate, 90 on the side wall, and 6 on the cowl. Details of the P_w distributions will be discussed later in this paper by comparing them with those by the CFD. The pressure drag was obtained by summation of the streamwise component of the force on the area elements. The drag coefficients defined by the model cross section ($40W \times 50H$) and the dynamic pressure of the $M3.4$ outer flow are shown in Table 1, where the minus sign expresses drag on the model.

To evaluate the friction on the model, the skin-friction coefficient (c_f) must be known. Let us approximate the flow on the inner surfaces with the turbulent boundary layer on the flat plates. The c_f can be expressed by the Reynolds number and the Mach number, if effects of wall temperature are ignored. Denoting the influence index of the static temperature by α, the averaged c_f is written as

$$c_f = \frac{0.472\{1 + [(\gamma - 1)/2]M^2\}^{-\alpha}}{(\log Re_L)^{2.58}} \tag{1}$$

Table 1 Comparison of drag coefficients found from the wall pressure measurement and the CFD

Row	Components (A)	Experiment			CFD			Deviation, %		
		Cd_p (B)	Cd_f (C)	Total (D)	Cd_p (E)	Cd_f (F)	Total (G)	Cd_p (H)	Cd_f (I)	Total (J)
1	Inner flow									
2	Inlets	−0.193	−0.015	−0.208	−0.185	−0.019	−0.204	−4.1	24.3	−2.1
3	Combustor	0.009	−0.007	0.002	0.009	−0.008	0.001	0	14.4	−50.2
4	Diverging section and nozzle	0.126	−0.018	0.108	0.117	−0.026	0.091	−7.3	45.5	−16.0
5	Cowl	0	−0.006	−0.006	0	−0.007	−0.007	——	20.7	20.7
6	Total (inner flow)	−0.058	−0.046	−0.104	−0.059	−0.060	−0.119	2.1	30.6	14.7
7	Outer flow									
8	Outer side wall	−0.041	−0.029	−0.070	——	——	——	——	——	——
9	Cowl	−0.011	−0.011	−0.023	——	——	——	——	——	——
10	Total (outer flow)	−0.052	−0.041	−0.093	——	——	——	——	——	——
11	Total	−0.110	−0.087	−0.197	——	——	——	——	——	——

The case of $\alpha = 0$ reduces to Schlichting's empirical formula[10] for incompressible flow, in which the local c_f is given as a function of Re. Schlichting introduces $\alpha = 1$ for compressible flow and the extended Frankl–Voishel formula[11] proposes $\alpha = 0.467$. The dynamic pressure can be calculated from the local M and P_w, if the boundary-layer approximation is applied. The frictional drag can be derived by summation of the tangential component of the stress force on wetted surface elements.

The local values of static and total pressure in the internal flow must be known to calculate the local M. Voland[5] used the static pressure measured to employ the boundary layer integral method in the inlet, and assumed an isentropic flow beyond the inlet throat. In this study, the whole internal flow in the model was approximated to be isentropic, because the compression ratio in this model is low and the loss in P_0 across the oblique shock waves was evaluated to be less than 10%. The error in the wall friction (υ_w) caused by that in P_0 arises from c_f given by Eq. (1) and q determined from the Mach number. The influence coefficient of P_0 to υ_w is given by

$$\frac{\Delta\, \upsilon_w/\upsilon_w}{\Delta\, P_0/P_0} = \frac{(1-\alpha)(\gamma-1)}{\gamma} + \frac{2}{\gamma M^2} \tag{2}$$

For example, substitution of $\alpha = 0.467$ and $M = 3.4$ yields 0.28 as the influence coefficient. This means that the overestimation of total pressure by 10% results in an overestimation for the real υ_w by 2.8%. Equation (2) shows that the isentropic flow can be approximated in scramjet engines with low compression ratios and that this approximation is improved at a higher Mach number. Thus, the local M was evaluated by the isentropic relation between the P_0 and P_w. The drag force on the model was evaluated by using $\alpha = 0.467$. However, it should be noted that the total pressure loss in inlets becomes significant with increasing Mach number. In addition, the installation of engine strut to promote flameholding also causes a large reduction of total pressure. Therefore, the isentropic approximation should be examined carefully in such cases.

In Table 1, the individual frictions are found to be small compared with those of pressure drag. However, the summation of these on the model surfaces becomes 0.087 [the (C)11 cell], [column (C), row 11 in Table 1], which is comparable with the pressure drag of 0.110 [(B)11]. Drags on the outer surfaces of the model were evaluated to be 0.052 [(B)10] for the pressure drag Cd_p and 0.041 [(C)10] for the frictional drag Cd_f. Consequently, the sum of Cd_p and Cd_f was estimated to be 0.197 [Cd in (D)11]. The friction occupied 44% of the total drag, and 47% of the total drag was produced on the outer surface of the model.

Consistency Between Experiments

The consistency between the P_w measurement and the force measurement was examined first. Figure 3 illustrates the results of the force measurement for the various configurations, where the drags of engine were calculated under the engine test condition in the RJTF (the model shown in Fig. 1 tested under $P_0 = 0.86$ MPa) on the right axis.

The top plate installed under the support strut had a value of $Cd = 0.048$. When the skin-friction coefficients were evaluated to be about $1.5E$-3 from Eq. (1), the value of $Cd = 0.048$ was produced by the support strut. Mounting the two side walls and the cowl on the top plate completed the engine module and increased the Cd to 0.230. The increment between Cd was found to be 0.182. When the side walls are attached to the top plate, the wetted surface on the top plate decreases and new surfaces exposed to the freestream are formed on the side walls and the cowl. Therefore, the change in the wetted area between the side wall on and off conditions was taken into account in the calculations of Cd. A small frictional drag of 0.0065 was produced in the inner surface of the top plate. We charged the top plate drag to the airframe in our convention, and excluded it from the engine internal drag.

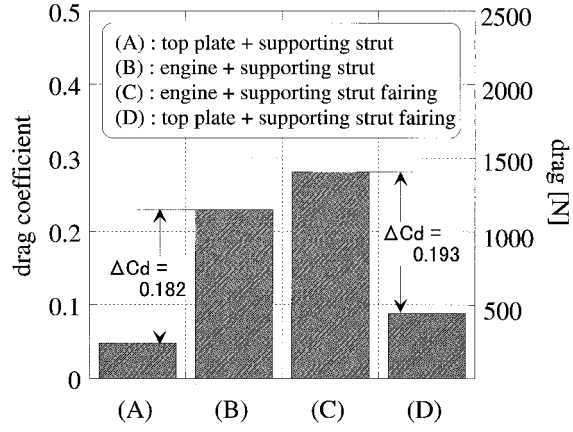

Fig. 3 Drag coefficients for various model configurations measured with the one-fifth-drag model.

When the blunt fairing was installed on the top plate to cover the strut, the Cd increased to 0.281, because the drag was transferred to the load cell. This configuration corresponds to the engine in the RJTF, where the total drag of 1430 N duplicates the engine drag, including the installation drag in the $M4$ RJTF testing. By removing the side walls and the cowl, the top plate with the supporting strut and the fairing showed a value of $Cd = 0.088$. This means that the increment caused by the side walls and cowl under the condition with the fairing was 0.193. Thus, the force balance experiments showed the drag of the model, excluding the top plate, to be $0.188 \pm 5\%$.

On the other hand, the model drag estimated from the pressure measurement is 0.197 [(D)11] in Table 1, which agrees with that derived from the force measurement within 4.6%. Because comparison between the pressure measurement and the CFD indicates that the pressure integration in Table 1 is accurate, as will be discussed later, we concluded that the discrepancy of 4.6% was a result of the overestimation of the friction drag by neglecting the pressure loss in Table 1.

We repeated the comparison between the pressure and the force measurements for the various model configurations of one side wall, the inlet segmented from the downstream parts, and the model with fuel struts. These comparisons prove that the results obtained in this wind-tunnel testing can be used as a benchmark for CFD studies.

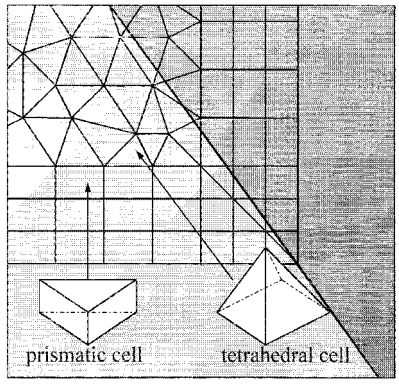

Fig. 4 Shapes of unstructured grid near engine wall employed in the newly developed Navier–Stokes code.

Navier–Stokes Computation

Internal flowfields of the scramjet engine are computed by solving the Reynolds-averaged Navier–Stokes equations.[9] The three-dimensional computational region inside of the engine is discretized by an unstructured hybrid grid, as shown in Fig. 4, for accurate and efficient computations as well as ease of grid generation for complex configurations.[12] The prismatic semistructured grid generated for viscous boundaries on the surfaces allows the control of minimum spacing required for resolving viscous sublayers, thus assuring the quality of the solution for high Reynolds number flows without decreasing the advantage of the flexible unstructured grid. The inner region of flowfield is covered with the tetrahedral cell, as shown in Fig. 3.

The solution algorithm used to compute the compressible Navier–Stokes equations is based on a cell-vertex, upwind, finite volume scheme for arbitrarily shaped cells.[13] The computational efficiency is drastically improved by the lower–upper symmetric Gauss–Seidel implicit method with a reordering algorithm for an unstructured hybrid grid. The turbulent kinetic viscosity is evaluated by a one-equation turbulence model proposed by Goldberg and Ramakrishnan.[14] This turbulence model does not need a procedure for searching along normal lines to walls as required in the Baldwin–Lomax algebraic model. Thus, it is suitable for an unstructured hybrid grid. The numerical accuracy of the flow solver was validated for several configurations related to scramjet engine computations.[9]

The skin friction and the heat flux along the wall are very sensitive to the local grid density near the wall. On the other hand, the total number of nodes is limited for realistic computations. In the present study, the grid size was optimized by calculating the boundary layer on a flat plate. The flow condition is similar to that of the scramjet engine. A grid with a minimum size of 2.5 μm accurately reproduced the law of the wall on the turbulent boundary layer. The calibration suggests that a grid of 2.5 μm is adequate to calculate the skin friction inside the engine.

A grid with 0.52 million nodes was distributed in the internal flow of the engine. The engine test condition was $M3.4$, $T_0 = 870$ K, $T_w = 290$ K, and $P_0 = 0.86$ MPa. In the experiments, the engine was installed and aligned with the wetted surface of the facility nozzle to simulate the ingestion of the boundary layer developed on the forebody of vehicles. To match the ingestion condition, the 99% thickness of inflow boundary layer on the top wall was assigned to occupy one-eighth that of the inlet height.

Results by CFD

Pressure Distributions

The pressure distributions between the one-fifth-scale mode and the full-scale engine without fuel injection agreed well. Therefore, Fig. 5 is a comparison of the pressure distribution obtained by CFD and that with the one-fifth-scale pressure model along the centerline on the sidewall. The streamwise distance is referenced to the inlet height (50 mm). Because the static pressure of the $M3.4$ flow ($P_0 = 0.86$ MPa) is 13 kPa, the wall pressure increases by the inlet

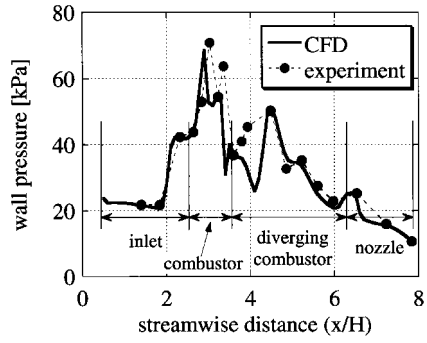

Fig. 5 Comparison of wall pressure distribution on the engine side wall.

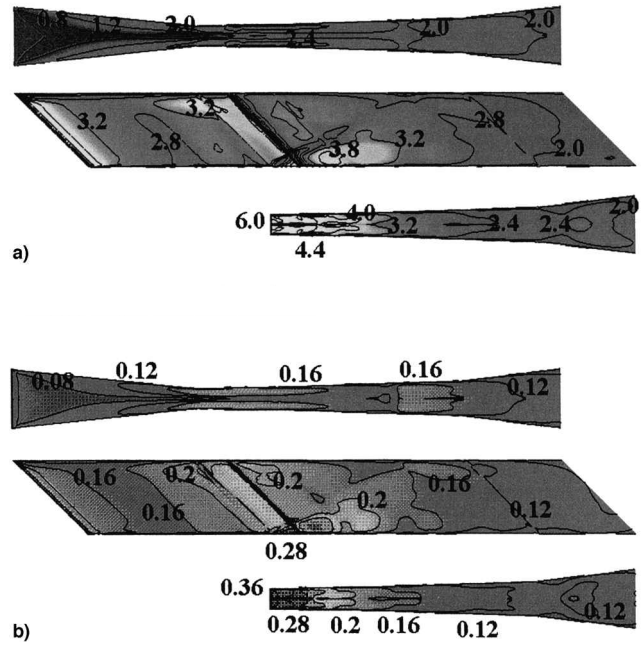

Fig. 6 a) Friction coefficient distributions on the engine wall by CFD (10^{-3}). b) Local heating rate distributions on the engine wall by CFD (MW/m^2).

wedge to 21 kPa and the reflected shock wave impinges at $x/H = 2.2$ in the figure. The reflected wave impinges again at $x/H = 2.9$, where the compression wave interacts with the expansion waves formed at the onset of the parallel section between the inlet and the combustor (the isolator).

At $x/H = 3.4$ in the combustor, there is a backward-facing step and a sharp pressure depression is observed. However, the wall pressure recovers to 40 kPa with the attached shock wave just downstream. The compression wave originating from the cowl arrives at $x/H = 4.4$.

The wall pressure derived by CFD around $x/H = 4$ disagrees with the experimental result. This region is the most converging section and the compression and expansion waves interact here. A finer grid in the streamwise direction is required. However, Fig. 4 indicates good agreement between CFD and the experiments and promises high accuracy of pressure drag evaluation.

Wall Friction and Heat Flux

A contour map of the c_f is shown in Fig. 6a, where c_f is defined using the dynamic pressure in the incoming flow and shown in units of 10^{-3}. The higher value found on the side-wall leading edge is a result of the undeveloped boundary layer. The friction is large in the diverging combustor section near the cowl because of the flow compressed by a shock wave generated at the cowl. The decelerated flow region in the combustor is occupied by the lower friction coefficient.

Because the top plate is covered with an ingested thick boundary layer, the friction coefficient at the leading edge is low (3×10^{-4}). Figure 6a indicates corner flow between the top plate and the side plate with higher shear. Although the corner flow by side walls develops downstream, the spanwise variation of c_f is small on the top plate.

CFD computation was conducted for the isothermal wall with a temperature of 290 K, and the heating rate distributions are illustrated in Fig. 6b. The distribution inclined by 45 deg in the inlet indicates that there was an impinging shock wave. The high heat flux of 0.28 MW/m^2 found near the leading edge on the sidewall is attributed to the corner vortex induced by the shock wave from the leading edge of the cowl. The highest heating rate attained a level of 0.6 MW/m^2 at the leading edge of the cowl. The strong shock wave from the cowl results in a region with a high heating rate near the cowl in the diverging combustor section.

On the top plate, a region with a higher heating rate of 0.16 MW/m^2 is formed upstream of the nozzle. This is generated by the impinging shock from the cowl. This shock heating is favorable for combustion. Autoignition and flameholding of H_2 were observed at this shock-impinging location in the $M6$ engine testing. The typical heating rates on the top plate vary from 0.1 MW/m^2 in the central inlet to 0.16 MW/m^2 in the shock-impinging region.

Comparison of Engine Drag

Itemization of Engine Drag

Drag produced in the engine components is itemized and compared with the experimental data in Table 1. Column (E) shows the pressure drag and column (F) denotes the frictional drag derived by CFD. The sum of these two drags is given in column (G). The experimental counterparts are shown in columns (B), (C), and (D). Columns (H), (I), and (J) indicate the deviations of the CFD from the P_w experimental results.

Column (B) reveals that a large pressure drag of -0.193 was produced in the inlet section. However, the compressed air delivered thrust in the diverging combustor and the nozzle sections (0.126), and the resultant pressure drag was found to be 0.058. The small thrust found at the combustor consisting of parallel duct was caused by the backward-facing steps.

Integration of the wall pressure obtained by CFD result in a pressure drag of 0.185 [(E)2] in the inlet section and a thrust of 0.117 [(E)4] downstream. The resultant drag was found to be 0.059 [(E)6]. CFD duplicates the pressure drag measured in experiments within 2.1% [(H)6]. Thus, the discrepancy between CFD and the experimental findings was small for the pressure force.

Friction derived from the wind-tunnel tests totaled 0.046 [(C)6]. On the other hand, the CFD value predicted 0.060 for the total friction of the model internal flow, and overestimated the friction by 31% [(I)6]. The friction in the diverging combustor section and the nozzle was greater than the experimental value by 46% [(I)4]. The total drag coefficients was evaluated to be 0.104 [(D)6] by the experiments and 0.119 by CFD [(G)6]. Consequently, the discrepancy in the total drag between the P_w measurement and the CFD was 15% [(J)6] in Table 1, if the internal drag evaluated from the wall pressure was employed as the reference.

The discrepancy in the inlet was only 2% [(J)2]. The large value of 50% in the combustor [(J)3] was caused by the small denominator (0.002). Greater discrepancy was found in the downstream sections of the model. Because the flow Reynolds number is fairly high in the wind-tunnel experiments, the possibility of relaminarization in the downstream region is neglected. We consider that the discrepancy is caused by error accumulated as a result of the limited grids in the streamwise direction in the engine internal flow. Optimization of grid distributions of the streamwise and the transverse directions is needed.

Voland[5] reported a higher internal drag of 0.150 for the NASA Lewis Research Center's scramjet in the $M6$ freestream. The higher value may be attributed to their higher compression ratio consisting of a 30-deg swept leading wedge and 10-deg compression surfaces in the engine tested. Force balance measurement of a scramjet engine with a fuel strut in the $M7$ test facility can be found in Ref. 15.

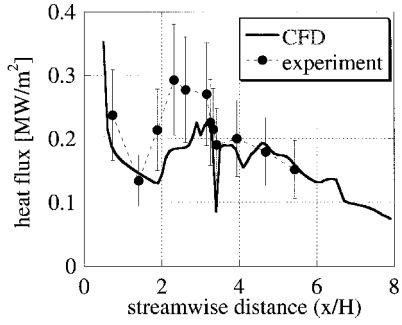

Fig. 7 Comparison of heating rate measured in engine testing and CFD results.

Calibration by Heat Flux Measurements

Direct measurement of local c_f in engine configurations is difficult. An example of the measurement of c_f using Preston tubes is presented by Yanta et al.[16] for an inward-turning scoop inlet at $M4$. Hazelton et al.[17] applied a skin friction gauge in an $M6$ scramjet inlet component test. In this study, the reliability of c_f data obtained by CFD was examined by heat flux measured in engines under no-fuel conditions.[18]

A comparison with the heating rate measured along the centerline of the side wall is shown in Fig. 7. The experiments were performed by a heat-sink-typeengine, in which thermocouples were embedded 1 mm deep in the 20-mm-thick copper walls. The heating rates were calculated using the temperature histories when the facility nozzle flow was changed from $T_0 = 290$ to 870 K. We evaluated an error in the measured heating rate to be 30% from the repeatability of differentiated temperature data.

In Fig. 7, the heating rate is illustrated by the broken line with the error bars. It indicates a high value of 0.28 MW/m^2 at the exit of the inlet ($x/H = 2.3$) and decreases to 0.2 MW/m^2 in the combustor ($x/H = 3$). The heat flux decreases to 0.15 MW/m^2 downstream in the combustor ($x/H = 4.5$). The heat flux derived by CFD (solid line) is compared with experiments in Fig. 7. The high heating rate at the leading wedge is attributed to the developing boundary layer. The bulge between $x/H = 2$ and 3 corresponds to the exit of the inlet, and the dip at $x/H = 3.2$ is caused by the local separation of flow at the backward-facing step. Thus, the CFD result for the wall heating rate agrees with the experimental result. This shows that the wall friction estimated by the CFD is also reliable.

In spite of the validation of the CFD result, there is a fairly large discrepancy in Cd_f (column I) in Table 1. One possible cause of this discrepancy may be that the wall conditions mismatched between the wind-tunnel experiments and the CFD. In the subscale wind tunnel, the air total temperature is 290 K. The flow can therefore be approximated to be adiabatic for the model with the room temperature, whereas the CFD computations and the heating rate measurements in engine testing were carried out at $T_0 = 870$ K and $T_w = 290$ K. Therefore, the engine wall should be treated as a cooled wall in the latter case. Cooling of walls increases the density near the walls and results in increased skin friction. On the other hand, the skin friction decreases on the adiabatic wall and heated walls may cause flow separation.[19–21] In our Mach 5.4 (flight Mach number 6) and 6.7 (Mach 8) tests employing a heated air with 600 K, the drag coefficients of the one-fifth-subscale model gradually decreased about 10% as the metal temperature increased. In addition, our CFD also indicated the reduction of c_f and a small separation bubble on the top wall, if the adiabatic wall condition is imposed in the Mach 4 calculations. Thus, the heat transfer to the engine walls might be one reason why CFD yielded greater frictional drag in Table 1.

External Drag and Internal Thrust

The drag on the external walls of the engine is evaluated in rows 8–10 in Table 1. The two outer wedges in the side plates produced

the large pressure drag of 0.041 [(B)8]. The pressure drag by the external flow was 0.052 [(B)10] and the sum of Cd_p and Cd_f was found to be 0.093. Figure 2 shows that the model drag with the fairing was 0.281 and that the drag resulting from the top plate, the supporting strut, and the fairing was 0.088, which corresponds to the installation drag. Thus, the engine installed on the supporting strut in freejet-type wind tunnels is subjected to an excessively large external drag, as reported in Ref. 22. Thus, the drag indicated by the load cells can be divided into three equal parts: one-third from the supporting strut with the fairing, one-third from the external walls, and one-third from the internal walls of the engine in the $M4$–RJTF testing.

Scramjet thrust performance has generally been based on parameter ΔF, which is defined as the thrust increment in the axial force with and without fuel injection. Because engine performance is determined by the impulse functions of the inflow stream tube captured by engines, only the internal drag $D_{\text{int}} = 490$ N of the engine drag of 1430 N in Fig. 3 should be included when discussing the engine internal performance as long as the external drag remains unchanged when fuel is injected into engines. Thus, overall thrust performance is the change in internal thrust, which is related to ΔF by $T_{\text{int}} = \Delta F + D_{\text{int}}$.

The force measurement system mounting the H_2-fueled scramjet engine in the RJTF indicated $F_{\text{LC}} = -1430$ N without fuel injection and -90 N with a fuel injection of 90 g/s under $M4$ flight conditions. This implies $\Delta F = 1340$ N. Adding $D_{\text{int}} = -490$ N to the ΔF, the internal thrust was found to be $T_{\text{int}} = 850$ N. This internal thrust performance corresponds to a specific impulse of about 10 km/s, based on the H_2 fuel rate.

Because inlet spillage is essential for starting engines with the side-wall-compression-type inlets, two drags: the additive drag associated with the curved, nonphysical stream tube and the side-wall drag on the internal inlet surface that is outside of the captured stream tube, have been included in the preceding internal drag. These drags are conventionally charged to the airframe.[6] In the convention, the net thrust and specific impulse might be slightly higher than the previously mentioned internal values. Similar calculations of thrust performance were done under $M6$ flight conditions.

Conclusions

The wall pressure distributions inside the engine and the engine drag were measured by using one-fifth-subscale models under $M4$ flight conditions without fuel injection. These data were compared with those of CFD, employing a new, unstructured code. These independent measurements led to the following conclusions:

1) The pressure and frictional drags were evaluated from the wall pressure measurements for comparison with the drag measurement. The model drags estimated by these two measurements agree within 5% and the accuracy of the wind-tunnel testing was confirmed.

2)CFD reproduced the pressure drag found experimentally within 2%. However, the total drag differed from that of the experiment by 15%, if the wall pressure measurement was chosen as the reference. This discrepancy was because of that in the friction estimation.

3) The heat flux measured on the engine wall suggested that CFD properly evaluated the friction on the model. The discrepancy in drag estimation may have been caused by the mismatched wall conditions.

4) These studies revealed that two-thirds of the total drag measured in the freejet engine tests was produced by the external flow in the RJTF. Excluding the external drag, the internal thrust delivered with H_2 combustion was estimated to be 850 N, and the specific impulse of the engine was found to be about 1000 s under the $M4$ flight condition.

References

[1]Kanda, T., Hiraiwa, T., Mitani, T., Tomioka, S., and Chinzei, N., "Mach 6 Testing of a Scramjet Engine Model," *Journal of Propulsion and Power*, Vol. 13, No. 4, 1997, pp. 543–551.

[2]Mitani, T., Hiraiwa, T., Sato, S., Tomioka, S., Kanda, T., and Tani, K., "Comparison of Scramjet Engine Performance in Mach 6 Vitiated and Storage-Heated Air," *Journal of Propulsion and Power*, Vol. 13, No. 5, 1997, pp. 635–642.

[3]Tani, K., Kanda, T., Sunami, T., Hiraiwa, T., and Tomioka, S., "Geometrical Effects to Aerodynamic Performance of Scramjet Engine," AIAA Paper 97-3018, July 1997.

[4]Guy, R. W., Torrence, M. G., Sabol, A. P., and Mueller, J. N., "Operating Characteristics of the Langley Mach 7 Scramjet Test Facility," NASA TM-81-929, March 1981.

[5]Voland, R. T., "Methods for Determining the Internal Thrust of Scramjet Engine Modules from Experimental Data," AIAA Paper 90-2340, July 1990.

[6]Covert, E. E. (ed.)., *Thrust and Drag*, Vol. 98, Progress in Astronautics and Aeronautics, AIAA, New York, 1985, pp. 170, 171.

[7]Duman, E. F., Sekar, B., and Wolff, J. M., "Two- and Three-Dimensional Viscous Analysis of High Speed Inlets and Comparison with Experimental Data," AIAA Paper 97-3273, July 1997.

[8]Barber, T. J., and Cox, G. B., Jr., "Hypersonic Vehicle Propulsion: A Computational Fluid Dynamics Application Case Study," *Journal of Propulsion and Power*, Vol. 5, No. 4, 1989, pp. 492–501.

[9]Kodera, M., Nakahashi, K., Hiraiwa, T., Kanda, T., and Mitani, T., "Scramjet Inlet Flow Computations by Hybrid Grid Method," AIAA Paper 98-0962, Jan. 1998.

[10]Schlichting, H., *Boundary Layer Theory*, 6th ed., McGraw–Hill, New York, 1968, pp. 603, 676.

[11]Rubesin, M. W., and Varga, S. A., "An Analytical and Experimental Investigation of the Skin Friction of the Turbulent Boundary Layer on a Flat Plate at Supersonic Speeds," NACA TN 2305, Feb. 1951.

[12]Sharov, D., and Nakahashi, K., "Hybrid Prismatic/Tetrahedral Grid Generation for Viscous Flow Applications," *AIAA Journal*, Vol. 36, No. 2, 1998, pp. 157–162.

[13]Sharov, D., and Nakahashi, K., "Reordering of 3-D Hybrid Unstructured Grids for Lower–Upper Symmetric Gauss–Seidel Computations," *AIAA Journal*, Vol. 36, No. 3, 1998, pp. 484–486.

[14]Goldberg, U. C., and Ramakrishnan, S. V., "A Pointwise Version of Baldwin–Barth Turbulence Model," *Computational Fluid Dynamics*, Vol. 1, 1993, pp. 321–338.

[15]Guy, R. W., Torrence, M. G., Sabol, A. P., and Mueller N. N., "Operating Characteristics of the Langley Mach 7 Scramjet Test Facility," NASA TM 81929, March 1981.

[16]Yanta, W. J., Collier, A. S., Charles Spring, W., III., Boyd, C. F., and McArthur J. C., "Experimental Measurements of the Flow in a Scramjet Inlet at Mach 4," *Journal of Propulsion and Power*, Vol. 6, No. 6, 1990, pp. 784–790.

[17]Hazelton, D. M., Bowersox, R. D. W., Neumann, J. R., and Hayes, J. R., "Skin Friction Measurements in a Mach 6 Inlet Test," AIAA Paper 97-2884, July 1997.

[18]Hiraiwa, T., Sato, S., Tomioka, S., Kanda, T., Shimura, T., and Mitani, T., "Testing of a Scramjet Engine Model in Mach 6 Vitiated Air Flow," AIAA Paper 97-0292, Jan. 1997.

[19]Spalding, D. B., and Chi, S. W., "The Drag of a Compressible Turbulent Boundary Layer on a Smooth Flat Plate With and Without Heat Transfer," *Journal of Fluid Mechanics*, Vol. 18, Jan. 1964, pp. 117–143.

[20]Hopkins, E. J., and Inouye, M., "An Evaluation of Theories for Predicting Turbulent Skin Friction and Heat Transfer on Flat Plates at Supersonic and Hypersonic Mach Numbers," *AIAA Journal*, Vol. 9, No. 6, 1971, pp. 993–1003.

[21]White, F. M., *Viscous Fluid Flow*, McGraw–Hill, New York, 1974, pp. 645–647.

[22]Thomas, S. R., and Guy, R. W., "Scramjet Testing from Mach 4 to 20, Present Capability and Needs for the Nineties," AIAA Paper 90-1388, June 1990.